Image quality of the proton imaging from computer-simulated data

ZHANG Conghua HOU Qing GOU Chengjun WU Zhangwen*

Key Laboratory of Radiation Physics and Technology, Ministry of Education, Institute of Nuclear Science and Technology, Sichuan University, Chengdu 610064, China

Abstract In this paper, the proton image quality of three designed phantoms is studied by the Monte Carlo simulation tool FLUKA, and is compared with that of the photon, and electron imaging. The passages of parallel beams were simulated by the phantoms for protons, electrons and X-rays, and the fluence and energy spectra of exiting particles are recorded. The proton energy loss imaging has a high quality under low transmission proton fluence, and its quality is superior to that of electron and photon fluence. The results demonstrate that proton energy loss imaging is especially suitable for the samples of hundreds of nano-thicknesses.

Key words Monte Carlo method, Proton imaging, Image quality, Simulation image

1 Introduction

In contrast to radiographic imaging techniques of CT and TEM (transmission electron microscopy), which use X-rays or electron beams, proton imaging is an emerging technique for non-destructive analysis with high-contrast, low-dose, and low-noise[1–6]. It has been applied in material modification, composition analysis, and biological analysis[7–9], with a good prospect in proton therapy and proton CT[1].

In this paper, high energy proton beams are simulated for proton imaging by M-C code of FLUKA. The image quality was studied by proton fluence, energy fluence, and energy loss map.

2 Principle of proton imaging

Unlike X-rays and electrons, protons undergo large energy loss as they pass through a specimen. Proton imaging can be formed by using either proton fluence, the energy fluence or energy loss. Proton fluence is usually used to form image of large specimens[10], and the intensity of proton beam is attenuated within its range of 90–100%. The image pixel value can be written as:

$$f(x,y)=\int I(x,y,E)\mathrm{d}E \tag{1}$$

where, $I(x,y,E)$ is the proton fluence at energy (E) and position (x,y) in the detection plane. On constructing the image by energy fluence, the image pixel value is given by Eq.(2):

$$f_{\mathrm{E}}(x,y)=\int EI(x,y,E)\mathrm{d}E \tag{2}$$

Using the energy loss due to proton inelastic collisions with atomic electrons [11], a higher resolution than Eqs.(1) and (2) can be obtained by integrating the specific energy loss along the track length (l)[12].

$$\begin{aligned}\Delta E = E_0 - E &= -\int_0^L \mathrm{d}l(\mathrm{d}E(l)/\mathrm{d}l)\\ &= \int_0^L \rho(l)S(l,E(l))\mathrm{d}l\end{aligned} \tag{3}$$

where, E_0 is an initial energy and E is a final energy for incident proton, $\mathrm{d}E/\mathrm{d}x$ is a linear stopping power of the protons, $\rho(l)$ is density of the material at a length l. $S(l, E')$ is mass stopping power as a function of l, and $E(l)$ is the local proton energy.

Unlike X-ray or electron imaging, which is based on the exponential law of attenuation, proton imaging is complex and sensitive to the track length due to the stopping power in the specimen. If average

Supported by National Natural Science Foundation (No.10775101)

* Corresponding author. *E-mail address:* wuzhangwen@gmail.com

Received date: 2009-11-06

energy of the transmitted proton is $E_{av}(x,y)$, the image pixel value for energy loss is given by

$$f_{ED}(x,y) = E_0 - E_{av}(x,y) \tag{4}$$

where, $$E_{av}(x,y) = \frac{\int I(x,y,E)E\mathrm{d}E}{\int I(x,y,E)\mathrm{d}E}.$$

3 Simulation models

To compare the three methods of proton imaging, particle transport in three types of phantoms was simulated by MC code of FLUKA. Parallel beam incidence was used. The energy spectra and fluence of the transmitted particles were recorded by a linear pixel detector.

The water phantoms were the box water phantom (BWP), right angle wedge water phantom (RAWWP), and ladder-shaped water phantom (LSWP). The box water phantom (10 cm×10 cm×6 cm) contained a Φ2 cm×10 cm PMMA cylinder (Fig. 1). PMMA, in density of 1.18 g·cm^{-3}, is suitable for mass contrast to water. The BWP was irradiated by 120 MeV proton beams of 4 cm×0.4 cm. The traverse protons were detected by a 10 cm×0.4 cm linear pixel detector with 100 units.

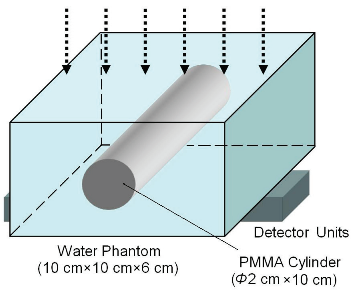

Fig. 1 Schematics of the box water phantom.

For comparison, 15 MeV electron beam and 20 keV photon beam were simulated. X-ray imaging is based on exponential absorption of incident photons in the material, and pixel value of photons is given by $f(x,y)=I(x,y)$, where $I(x,y)$ is the photon fluence at point (x,y). The electron absorption obeys the exponential law, too, but the process is determined by electron scattering along their paths in the material. The pixel value of electrons is $f(x,y)=I(x,y,E)$, where $I(x,y,E)$ is the electron fluence at energy E and point (x,y).

For all simulations in this work, 10^7 incident particles in vertical beam incidence were used.

The RAWWP (Fig.2) was a minute phantom in 800-nm height and 100 µm×100 µm transverse size. It was irradiated by 4 MeV proton beams, or 1 MeV electron beams, of 140 µm×1 µm in size. The linear detector had 140 units.

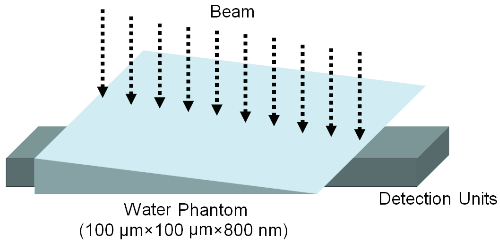

Fig. 2 Schematics of the right angle wedge water phantom.

The LSWP (Fig.3) for studying the imaging resolution and stability had ten steps, each of which was 1-nm high and 10-µm wide. It was irradiated by 4 MeV proton beams, or 100 keV electron beam, of 140 µm×1µm size. The detector had 140 units.

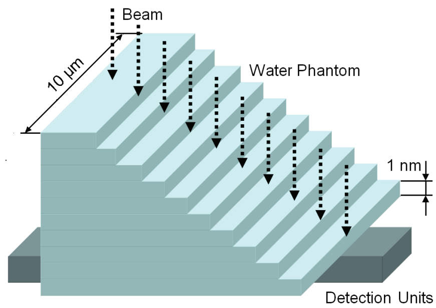

Fig. 3 Schematic of the LSWP in simulation.

4 Results and discussion

4.1 Box water phantom

Fig.4a shows the normalized fluence distribution along the linear detector for the traverse protons, electrons, and photons. Each detector unit corresponds to a pixel, and the vertical dots indicate the borders of the PMMA cylinder. The incident beam covers the 30th–70th pixels, and the PMMA cylinder, the 40th–60th pixels. The proton fluence distribution well represents the coverage of the incident beam and PMMA cylinder. However, because of severe scattering effect of the electrons, the electron fluence distribution is much wider than proton, spanning from the 1st to 100th pixel and the PMMA cylinder being not detectable. The X-ray has an arc-like fluence distribution in 40th–60th

pixel, reflecting clearly the cylinder size. Fig.4b shows the normalized distributions of the transmission fluence, energy fluence, and energy loss of the proton beam. The distribution of energy fluence and energy-loss depend obviously on the cylinder in the 40^{th}–60^{th} pixels. This means that improved contrast can be obtained using the energy fluence and the energy-loss, especially the latter, which has two sharp peaks at the 40^{th} and 60^{th} pixel, indicating an enhanced contrast of the cylinder boundary.

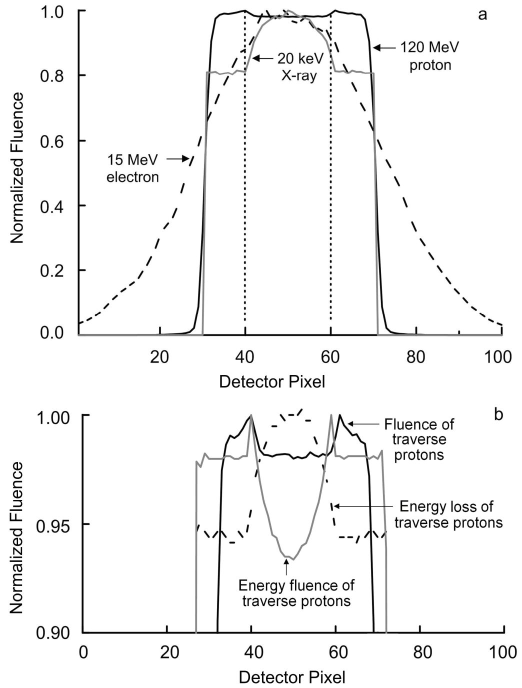

Fig.4 Distributions of transmission fluence of 120 MeV protons, 15 MeV electrons and 20 keV X-ray photons (a) from the box water phantom (6-cm thick, 10 cm×10 cm) containing a a Φ2 cm×10 cm PMMA cylinder, and distributions of transmission fluence, energy fluence, and energy-loss of the protons (b).

4.2 Right angle wedge water phantom

The RAWWP was irradiated by 4 MeV proton or 1MeV electron beams, but the phantom is too thin (800 nm) to cause any observable attenuation of the X-rays and form any contrast image. Fluence distribution of the unscattered electrons penetrating the RAWWP (Fig. 5 a) shows a curvatured wedge. The results indicate that the relationship between the electron fluence and the phantom thickness is not linear, since multiple scattering occurs as an electron penetrates the phantom, hence the need of a calibration to correct the non-linearity.

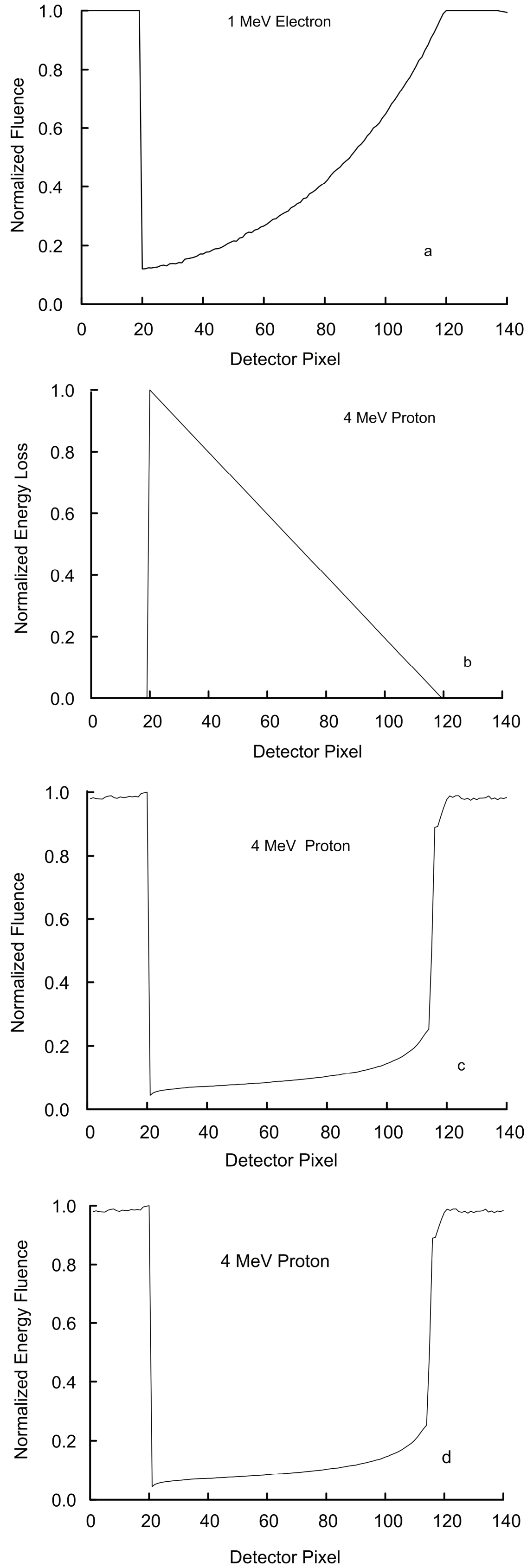

Fig.5 Electron fluence distribution (a) with the right angle wedge water phantom (800 nm thick,100 μm×100 μm), and distributions of proton energy loss(b), proton fluence (c) and proton energy fluence (d) with the RAWWP.

The distribution of proton energy loss (Fig.5b) reconstructs the wedge perfectly. In addition, this can be achieved with reduced sampling number of the incident protons. However, the distribution of proton fluence (Fig.5c) and proton energy fluence (Fig. 5d) failed to show the phantom wedge. These indicate that proton energy loss is linearly proportional to the phantom thickness, despite the multiple scattering of the protons, which affect the proton fluence and proton energy fluence, but not the energy loss.

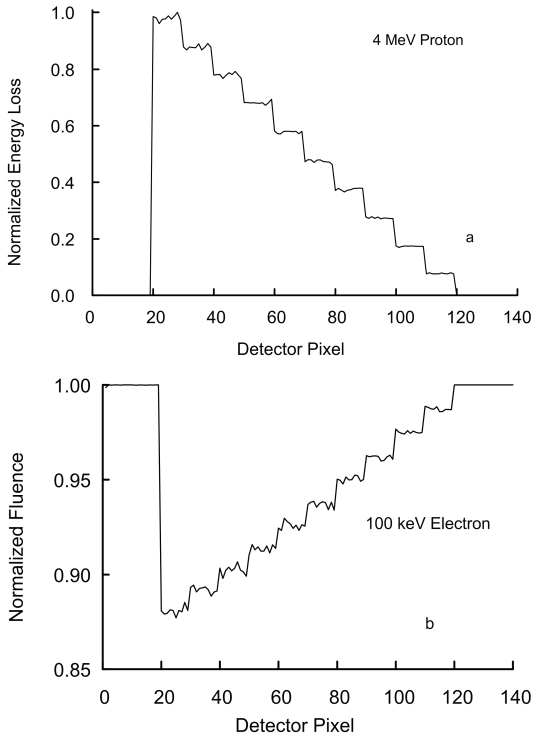

Fig.6 Distribution of proton energy loss (a) and transmission electrons (b) with the ladder-shaped water phantom with ten 10-nm steps.

4.3 Ladder-shaped water phantom

The LSWP was simulated with 4 MeV proton and 100 keV electron beams. Both distributions of the proton energy loss and transmission electrons are ladder-shaped (Fig.6), but the step edges in Fig.6b are almost smeared out by noise, especially in the thick parts of the LSWP, while the distribution of proton energy loss is consistent with the phantom shape throughout the phantom steps, and the image contrast keeps good quality with reduced number of incident proton, too. The distributions of proton fluence and proton energy fluence are not shown, because the phantom image cannot be extracted.

5 Conclusions

Proton imaging of three phantoms has been simulated by the FLUKA code, using the transmission proton beams, and compared with that of transmission electron and X-ray beams. Instructive information has been obtained for the imaging resolution and detection efficiency. For centimeter-scale samples, the imaging can be performed using energy fluence of the transmission protons to enhance the object boundaries. For nanoscale samples, imaging by energy loss of the proton beams is preferred, and number of the incident protons can be reduced. The results show that the proton energy loss imaging is the best choice for improving image contrast and reducing image noise.

References

1 Hartmut F.-W. Sadrozinski, Stephen G, *et al*. IEEE Trans Nucl Sci, 2004**, 51:** 3–9.

2 Adamsa F, Van V L, Barrettb R. Spectrochimica Acta Part B, 2005, **B60:**13– 26.

3 Pontau A E, Antolak A J, Morse D H, *et al*. Nucl Instrum Meth Phys Res B, 1989, **B40:** 646–650.

4 Hanson K M, Bradbury J N, Cannon T M, *et al*. IEEE Trans Nucl Sci, 1978, **NS-25:** 657–660.

5 Frank W. Nucl Instrum Meth Phys Res B, 1997, B130: 1–8.

6 Saint A, Bench G S, Cholewa M, *et al*. Nucl Instrum MethPhys Res B, 1991, **B56-57:** 717–721.

7 Formenti P, Breese M B H, Connell S H, *et al.* Nucl Instrum Meth Phys Res B, 1997, **B130:** 230–236.

8 Antolak A J, Bench G. S, Pontau A E, *et al.* Nucl Instrum Meth Phys Res A, 1994, **A353:** 568–574.

9 Schwertnera M, Sakellarioub A, Reinerta T. Ultramicroscopy, 2006, **106:** 574–581.

10 Cookson, D J A. Naturwissenschaften, 1974, **61:**184–191.

11 Kramer S L, Moffett D R, Martin R L, *et al.* Radiology, 1980, **135(2):** 485–494.

12 Hanson K M, Bradbury J N, Cannon T M, *et al.* Phys Med Biol, 1981, **26:** 965–983.